

Dissolution of Magnesium Oxide in Aqueous Acid: An Atomic Force Microscopy Study

Marco Fidel Suárez and Richard G. Compton*

Physical and Theoretical Chemistry Laboratory, Oxford University, South Parks Road, Oxford OX1 3QZ, U.K.

Received: May 5, 1998

The dissolution of the surfaces (100), (110), and (111) of MgO in aqueous hydrochloric acid is studied by in-situ AFM experiments in a flow cell with known hydrodynamics, which permits the modeling of the rate of proton transport to the solid surface. Comparison with directly measured rates of dissolution determined via monitoring the absolute height of the surface in real time shows that the dissolution of all three surfaces is a surface-controlled reaction. Examination of the surface morphology shows that the (100) plane dissolves via the growth of etch pits which are of circular or square shape depending on the acid concentration. In contrast, the (110) surface dissolves to form a corrugated surface of parallel ridges whose surfaces are predominantly composed of (100) planes. The (111) surface dissolves via triangular etch pits of a fixed orientation where (100) planes are partly re-expressed during the pit growth. These observations are in concordance with previous reports that the (100) plane is the most stable surface of MgO.

Introduction

A large number of industrial and natural processes involve the dissolution and growth of crystals from aqueous solution. Crystals are synthetically grown for use as electronic components, gems, reagents, and pharmaceuticals and are etched as a part of routine material evaluation. In nature, minerals form from some fluids but are attacked by others and lithification of sediments depends on a variety of growth and dissolution steps. The attempt to understand and quantify these diverse phenomena has led to a recent proliferation of dissolution-rate studies on solids.¹

The development of scanned probe microscopy and, specifically, atomic force microscopy (AFM) has yielded a wealth of new information on the structure, reactivity, and many other properties of surfaces and interfaces at high spatial resolution.² In particular, AFM has the potential to directly assess the validity of classical dissolution theories, for example, the Burton, Cabrera, and Frank model,³ at the atomic level by imaging the retreat of monatomic steps during the dissolution of a surface.

Traditionally, powders are used in measurements of dissolution in order to maximize surface area and, thus, the total rate of mass transfer. However, such measurements are hindered by the need to determine the surface area, the problem of surface area versus active site density, and the difficulties of preparation and reproducibility of particulates. In order to improve on this situation, Gratz⁴ developed the “negative crystal method” for measuring the dissolution rate of quartz in basic solution by observing the retreat velocity of nearly perfect crystal faces. In this approach the expansion of faceted depressions formed by the etching of surface microfractures was measured from AFM images. However, AFM experiments in stationary solution do not take into account depletion of the concentration at the solid–liquid interface of the different reacting species in the solution phase arising due to the consumption through the surface chemical reaction. Accordingly, under these conditions it is very difficult to make a rigorous study of the kinetics and mechanism of interfacial reactions.¹

To overcome reactant depletion problems in atomic force microscopy, two types of AFM flow cells have been designed.

One has recently led to in-situ studies of dissolution processes of calcite^{5,6} in which the hydrodynamics were uncertain. The other AFM fluid cell was designed by Compton and co-workers for the Topometrix TMX 2010 AFM instrument^{7–9} with a complete description of the hydrodynamics. The latter cell was designed by the addition of a new inlet port to a commercial fluid AFM cell, so that solution can be delivered through a precisely shaped and positioned stainless steel duct directly in front of the cantilever chip. The liquid jet is aligned parallel to the front of the cantilever support chip and transverse to the cantilever. This gives a partly free field flow, not confined except by the sample below and the cantilever chip to one side, so the flow pattern was complex but solved using a computational fluid dynamics program; the transport of the various species in the cell are defined, calculable, and controllable.^{7,8}

In this paper, we apply the hydrodynamic AFM cell to study the dissolution of the MgO crystal (100), (110), and (111) surfaces in aqueous acid. Understanding the surface properties and the dissolution mechanisms of the different crystallographic planes of MgO in acid conditions is crucial for a wide variety of processes, including, for example, corrosion,¹⁰ catalysis,¹¹ and drug design.¹² MgO is in widespread use as a substrate for thin film growth¹³ and radioactive waste storage.¹⁴

Experimental Section

A Topometrix TMX 2010 Discoverer atomic force microscope, operating in contact mode, was employed to image the surface of the solid substrates. A commercial Topometrix liquid cell¹⁵ was used, with some modifications^{7,8} to allow for controlled and modelable hydrodynamics, for in-situ AFM imaging. A gravity feed with an adjustable stopcock allowed control of the solution flow rate through the fluid cell. Pyramidal silicon nitride tips (Topometrix AFM probes 1520) were employed, and a scan area of $20 \times 20 \mu\text{m}$ was typically imaged. In all cases, two types of experiments were undertaken: (a) recording of conventional topographical images and (b) monitoring of the absolute average z -piezo voltage during the scanning. In the latter, calibration of the change of height with applied z -piezo voltage permitted real drops or increases

in the height to be measured. This calibration was achieved by imaging a Topometrix calibration grid, with a known precisely defined thickness of $2400 \text{ Å} \pm 8\%$, and measuring the z -piezo voltage changes between topographical maxima and minima. Using this procedure, a voltage–height conversion constant of $0.333 \pm 0.016 \text{ V } \mu\text{m}^{-1}$ was obtained. The flux of the reacted material could be determined through the z -piezo constant, assuming a density at 25°C of 3.58 g cm^{-3} for MgO .¹⁶ A series of images of the dissolving surfaces were then recorded continuously at 60 s intervals, corresponding to scan rate of $200 \text{ } \mu\text{m s}^{-1}$, and a resolution of 200×200 data points per image, in order to measure the increase or drop of the absolute height of the surface in real time. Measurements were made under ambient temperature conditions of $20 \pm 1^\circ\text{C}$. After AFM dissolution experiments, any surface damage at a macroscopic scale was characterized by using an optical microscope (OLYMPUS BH-2) at $400\times$ magnification.

Solutions were made using triply distilled deionized water purified with an Elgastat UHQ apparatus, which provided water with a resistivity greater than $10^7 \text{ } \Omega \text{ cm}$. AnalaR grade reagents NaCl , $\text{Mg}(\text{NO}_3)_2$, and HCl (36%) were purchased from BDH and MgO crystals supplied by CRYSTRAN Ltd. The latter were indexed and crystal faces assigned using standard methods by X-ray back-reflection. The crystals were cut parallel to the (100), (110), and (111) planes and polished mechanically for 3 h on a $6 \text{ } \mu\text{m}$ diamond solder lap, followed by 2 h on a $1 \text{ } \mu\text{m}$ solder lap before use. This procedure yielded smooth mirror-like surfaces. The quality of the surfaces was analyzed by AFM in air or in water prior to significant dissolution as discussed below.

Mathematical Simulation of MgO Dissolution Under Hypothetical Transport Control

For the mathematical simulation of the rate of MgO dissolution, if it were controlled by proton transport, the rate of mass transport of protons from the bulk solution to the crystal surface was described by the following time-dependent convective diffusion equation:

$$\frac{\partial c}{\partial t} = D_{\text{H}^+} \frac{\partial^2 c}{\partial y^2} - V_x \frac{\partial c}{\partial x} - V_y \frac{\partial c}{\partial y}$$

where x is the direction of the flow over the crystal surface, y the direction perpendicular to the surface, c is the concentration of protons, D_{H^+} is the proton diffusion coefficient, and V_x and V_y represent the solution velocity profile in the x and y directions. For the transport-controlled model, we assumed that the crystal face dissolution is controlled by the transport of protons from the bulk solution to the surface. This implies that the surface concentration of protons is zero. If we take the stoichiometry of the reaction into account, two protons are consumed for each Mg^{2+} dissolved and the flux of magnesium ions from the crystal surface can be expressed as

$$j(\text{mol cm}^{-2} \text{ s}^{-1}) = D_{\text{Mg}^{2+}} \left(\frac{\partial [\text{Mg}^{2+}]}{\partial y} \right)_{y=0} = -\frac{1}{2} D_{\text{H}^+} \left(\frac{\partial [\text{H}^+]}{\partial y} \right)_{y=0}$$

The mass transport for this model was solved for the steady-state mass transport using the backward-implicit finite difference

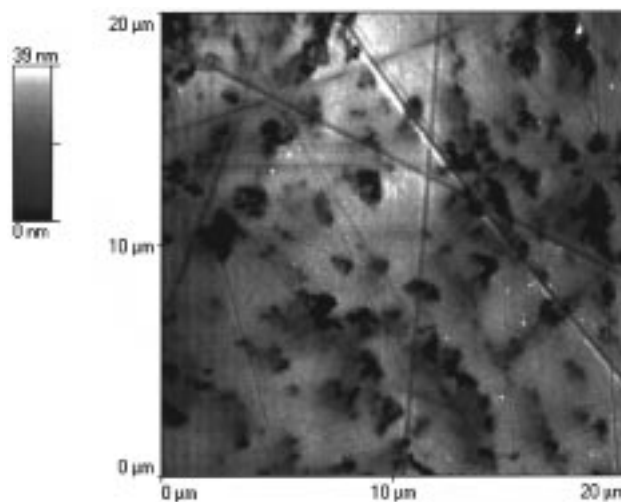


Figure 1. AFM image measured in air of the (100) plane of MgO after polishing.

method¹⁷ with the solution velocity profiles characteristic of the AFM flow cell as reported by Coles et al.^{7,8} and a value of $9.3 \times 10^{-5} \text{ cm}^2 \text{ s}^{-1}$ for the proton diffusion coefficient (D_{H^+}).¹⁶

Results

After polishing, AFM imaging in air of the (100) planes showed the surfaces to be smooth: the maximum difference in height over an area of $20 \times 20 \text{ } \mu\text{m}$ was typically around 40 nm. Figure 1 shows a representative part of a (100) plane; scratch lines and some roughness are present on the surface. We could not image the (110) and (111) surfaces in air, probably because of high capillary forces induced by the adsorption of water, but the initial in-situ images of these surfaces during the dissolution experiments gave surfaces with a maximum difference in height of 200 nm over an area of $20 \text{ } \mu\text{m} \times 20 \text{ } \mu\text{m}$.

Next, we measured the dissolution of the (100), (110), and (111) surfaces in flowing aqueous solutions of HCl at concentrations between 0.01 and 0.1 M. This range of concentration was selected because the rate of dissolution and the topographic changes of MgO surfaces were appropriately fast to be measured by the AFM flow cell method. At lower concentrations, the dissolution of MgO was too slow to be studied by the AFM technique. At higher acid concentrations, it was very difficult to record images continuously for a period in excess of 15 min, because of the formation of H_2 bubbles in the cell due to the dissolution of the tip holder.

Figure 2 shows representative optical and AFM images of the different surface morphologies when the (100) plane was dissolved in different concentrations of aqueous HCl . Circular pits were formed during the dissolution in 0.1 M HCl , and the rate of pit growth (diameter growth) was found to be $2.2 \pm 0.3 \text{ nm s}^{-1}$. Square pits, with sides growing parallel to the direction $\langle 110 \rangle$, with rounded corners were formed under 0.025 M HCl . Perfect $\langle 110 \rangle$ square pits with sides that grew at a rate of $1.7 \pm 0.1 \text{ nm s}^{-1}$ were seen under 0.010 M HCl . The average depth of the pits in all cases was between 200 and 400 nm. These observations are qualitatively consistent with the report of Sangwal and Sutaria¹⁸ who did ex-situ optical studies of etch pit morphology after dissolution under wide variety of conditions.

In addition, for the case of 0.100 and 0.025 M HCl , we observed the formation of small hillocks over the surface. In

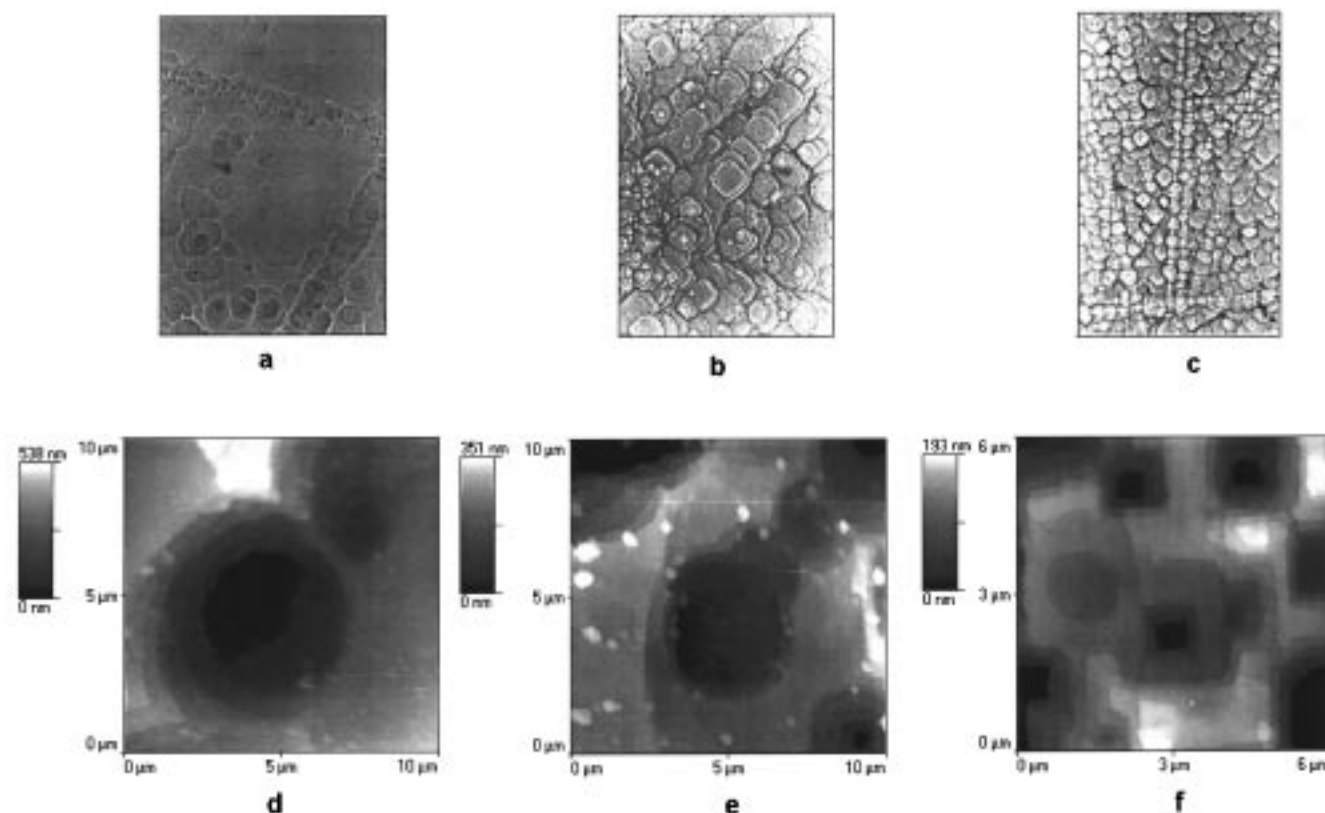


Figure 2. Optical (top) and in-situ AFM (bottom) images of the etch pit morphology during the dissolution of the (100) plane of MgO in hydrochloric acid: (a and d) 0.1 M HCl, (b and e) 0.025 M HCl, (c and f) 0.01 M HCl. The magnification of the optical images is $400\times$.

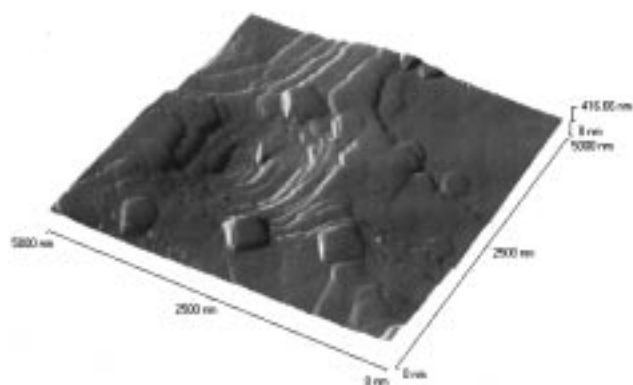


Figure 3. In-situ AFM image of the etch pits and hillocks on the (100) MgO surface formed during dissolution in 0.025 M HCl.

0.100 M HCl, the shape of the hillocks were conical, but in 0.025 M HCl, the shape was more regular, in the form of parallelograms or truncated square pyramids oriented in the $\langle 100 \rangle$ direction, as shown in Figure 3. The formation of these hillocks has been reported before by Ghosh¹⁹ but in concentrated sulfuric and orthophosphoric acid conditions. These hillocks are probably the result of the re-precipitation of MgO or $\text{Mg}(\text{OH})_2$ as suggested by Sangwal and Arora.²⁰

We turn next to the (110) and (111) surfaces. Figure 4 shows the formation of ridges in the direction $\langle 110 \rangle$ with slopes between 30° – 45° during the dissolution of the surface (110) in 0.01 M hydrochloric acid. The cross-sections in Figure 4 show the evolution of the ridges over a period of 82 min. At the beginning of the dissolution, the height of the ridges is between 0.1 and 0.4 μm , but over a period of 82 min of reaction, they become more developed, attaining between 1 and 2 μm in height. The number of ridges per unit area increased with the concentration of the acid, as shown in Figure 5. In our

experiments we did not observe the formation of pits in the (110) surface during acid dissolution as claimed by Sangwal and Sutaria¹⁸ on the basis of ex-situ measurements.

During in-situ acid dissolution of the (111) plane of MgO, we observed the formation of triangular pits and small irregular hillocks, as shown in Figure 6, consistent with an independent observation made by Sangwal and Sutaria.¹⁸ The orientation of the ridges in the (110) surface and the triangular pits on the (111) surface have the relationship to the MgO crystal structure as shown in Figure 7.

The topography of the (110) and (111) surfaces suggest that these planes dissolve in such a way as to form the (100) plane during acid dissolution; this is consistent with the expectation that this is the most stable plane. Moreover, it has been demonstrated experimentally¹¹ and rationalized by theoretical simulations²¹ that even in air or in vacuum the MgO planes with Miller indices higher than (100) facet into steps of (100) surfaces with depths of the order of 20 Å. For the case of (110) and (111) surfaces, the shape of the faceted surfaces is shown in Figure 7. The relationship to the morphology of the surfaces developed under acid dissolution is clear.

For the recording of kinetic dissolution data, the dissolution rates of the surfaces were measured not at the beginning of the dissolution but under conditions approaching a steady state, where the z -piezo voltage changed linearly with time, as illustrated in Figure 8. Table 1 summarizes the surface average rates of dissolution of the MgO faces (100), (110), and (111) in aqueous acid. The dissolution of the (100) and (111) planes change little with increasing acid concentration between 0.01 and 0.1 M. These results are in concordance with previous reports of acid-induced MgO dissolution. For instance, Guspiel and Riesenkauf found that at concentrations of H_2SO_4 between 0.1 and 2 M, the dissolution of MgO was constant,²² while Jones

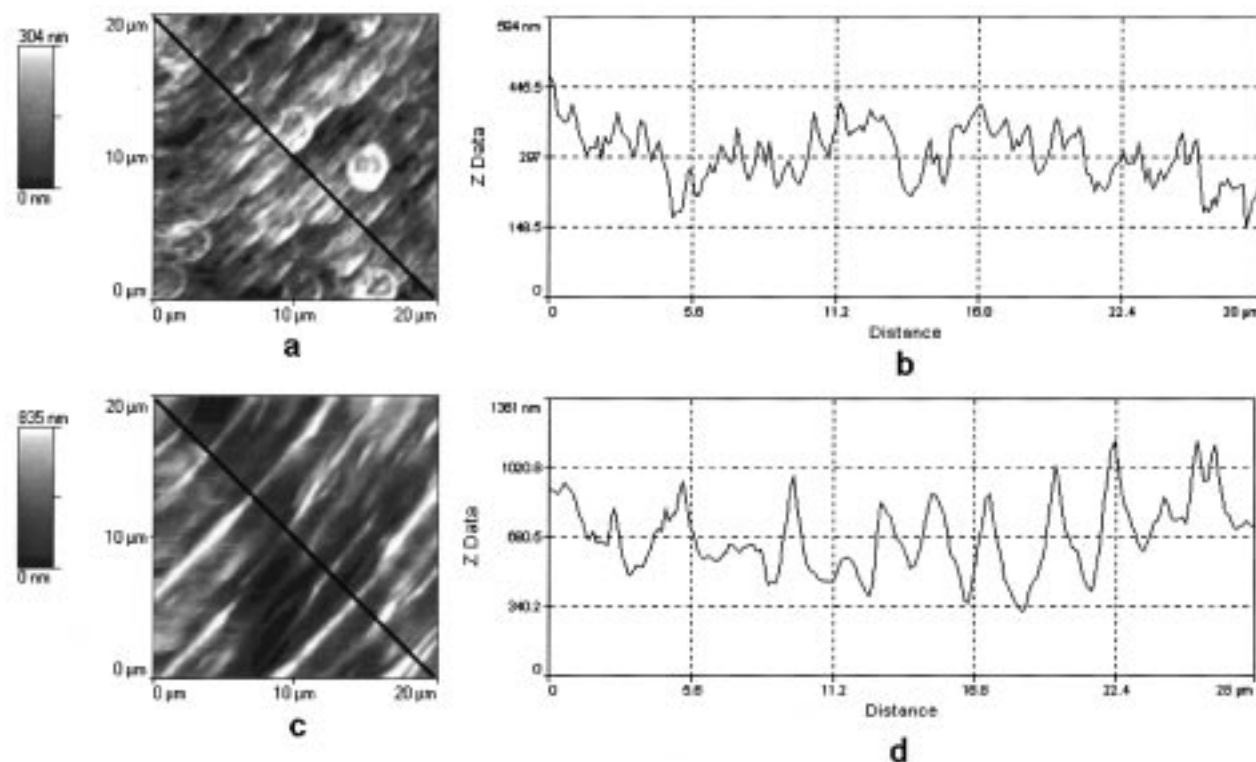


Figure 4. In-situ AFM images (left) and cross-sections (right) of the evolution in time of the ridged shapes formed on the (110) surface of MgO during dissolution in 0.01 M HCl: (a and b) at the beginning of the dissolution, (c and d) after 82 min of reaction.

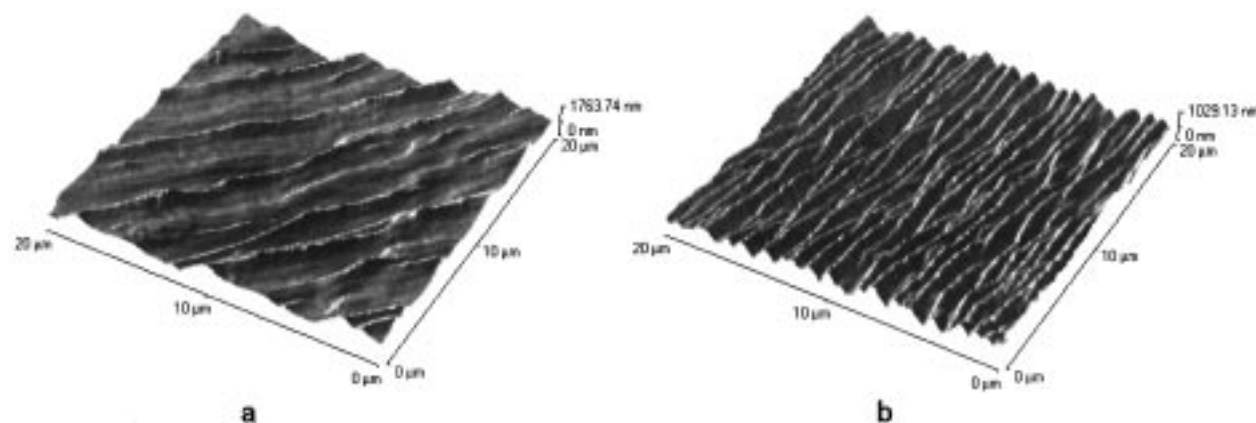


Figure 5. In-situ AFM images of the ridges formed on the (110) surface of MgO during dissolution in (a) 0.01 M HCl and (b) 0.1 M HCl.

et al. found that the initial rate of dissolution of a suspension of nearly perfect (100) MgO surfaces of smoke cubes was independent of pH in the range 2.0–3.5.^{14,23}

The rates of dissolution for all planes in 0.01 and 0.100 M HCl are 10 and 100 times, respectively, lower than the dissolution rates predicted by the mathematical simulation of the H^+ transport control model, as shown in Figure 9. This clearly demonstrates that the dissolution of MgO is *surface controlled*. Further evidence for the surface control comes from the observed flow rate dependence of the dissolution rate, as shown in Figure 9, where the dissolution rates of the (100) and (111) surfaces were independent of the solution flow rate. Moreover Table 1 shows that all three planes dissolve, to within less than an order of magnitude, at broadly similar rates. This is consistent with the notation developed above that (110) and (111) surfaces facet to develop (100) planes. The small variation of the dissolution rates may reflect the microfaceting morphology of each individual surface and/or the real surface area which is in contact with the solution.

We consider next the effect of added salts on the observed dissolution rates. Table 1, which gives surface-averaged dissolution rates, and Table 2, which gives rates of pit growth, both show some small but real and significant suppression of dissolution by the added salts NaCl and $Mg(NO_3)_2$. At the same time, significant topographic changes are induced by Mg^{2+} ion on the (110) surface. In the presence of this ion, this surface did not form a corrugated surface composed of (100) planes; instead, the dissolving surface was as shown in Figure 10, which shows a much more irregular and rougher surface. Similar experiments on the (100) plane also revealed noticeable effects of added salts. For both NaCl and $Mg(NO_3)_2$ there was a significant reduction of the velocity of pit growth, as given in Table 2, although the shape of the square pits did not change.

Discussion

The experimental results above clearly indicate that the dissolution from all planes is much slower than the rate of

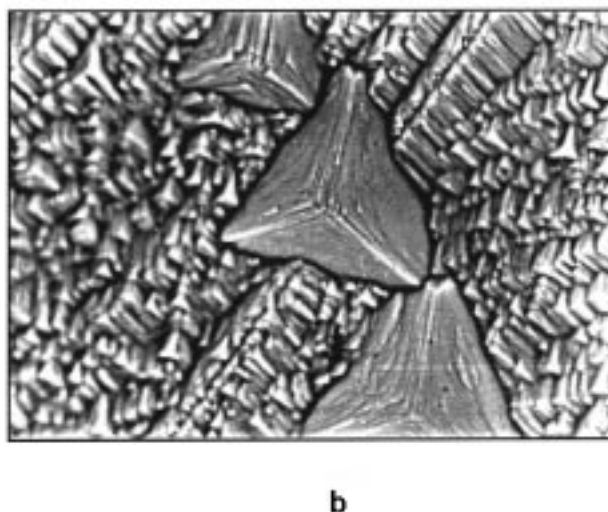
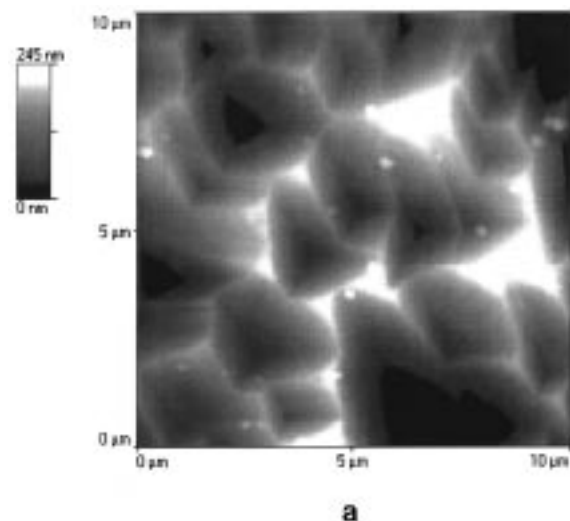


Figure 6. (a) In-situ AFM image and (b) 400× optical images of the triangular etch pits formed on the (111) surface of MgO during dissolution in 0.01 M HCl.

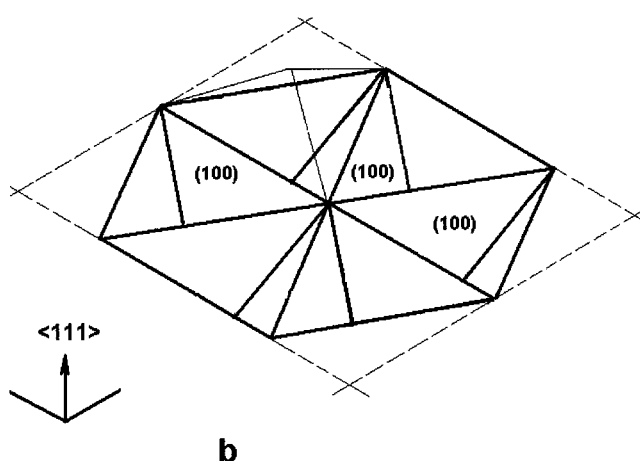
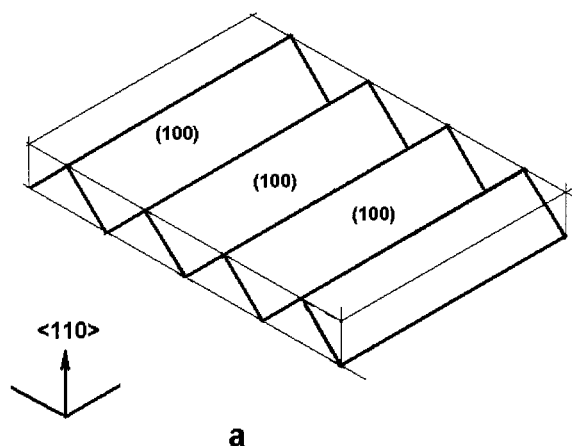


Figure 7. Schematics of (a) the (110) and (b) the (111) surfaces of MgO developed during dissolution in aqueous acid.

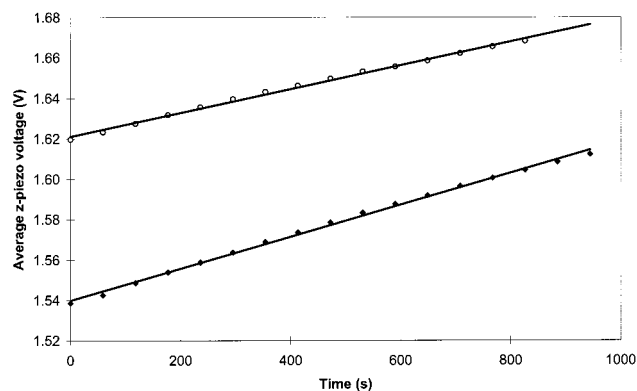


Figure 8. Change of the average z-piezo voltage of a AFM image of $20\ \mu\text{m} \times 20\ \mu\text{m}$ in time during in-situ dissolution of the plane (100) in 0.01 M HCl. The solution flow rate was $1.4 \times 10^{-2}\ \text{cm}^3\ \text{s}^{-1}$, and the scan rate was $200\ \mu\text{m}\ \text{s}^{-1}$. The plot shows two different sequences measured under the same experimental conditions.

transport of protons to the interface. As inferred above, this unambiguously demonstrates that the dissolution rate is surface controlled. It is interesting to consider the likely processes controlling the rate of MgO dissolution under the conditions of our study. We note first that the surface hydration is known to be fast^{24,25} and second that the pH insensitivity of the reaction, as seen above and independently,^{14,22,23} implies that while the reaction is proton driven, the coverage of absorbed protons^{26,27}

TABLE 1: Dissolution Rates of the Surfaces (100), (110), and (111) of MgO in Aqueous Hydrochloric Acid^a

surface	[HCl]				
	0.01 M				
	acid only	+0.1 M NaCl	+0.01 M $\text{Mg}(\text{NO}_3)_2$	0.025 M acid only	0.1 M acid only
(100)	1.9	0.8	1.4 ^b	1.4	1.5
(110)	5.0 ^b	1.9	2.3	4.6	2.4
(111)	0.8				0.4

^a The dissolution rates are expressed in $10^9\ \text{mol}\ \text{cm}^{-2}\ \text{s}^{-1}$. The likely error is $\pm 0.3 \times 10^{-9}\ \text{mol}\ \text{cm}^{-2}\ \text{s}^{-1}$. ^b This value is reported for a specified flow rate of $1.9 \times 10^{-2}\ \text{cm}^3\ \text{s}^{-1}$ because at this concentration the dissolution rate decrease slightly at slower solution flow rate.

must be sufficiently high that the rate-determining process involves the detachment of dissolution products from the crystal surfaces. Accordingly, we focused on the etch pit morphology in light of the simultaneously determined dissolution rate data.

By etching the (100), (110), and (111) planes with different acids, a change in the orientation of etch pits has been reported.^{18–20} Our results show that in the range of concentrations between 0.01 and 0.1 M of HCl, the pit morphology on the (100) plane changes from square <110> pits to circular pits with an increasing concentration of acid. Moreover, the rate of growth of the diameter of the circular pits is higher than the rate of growth of the sides of the square pits, although the total

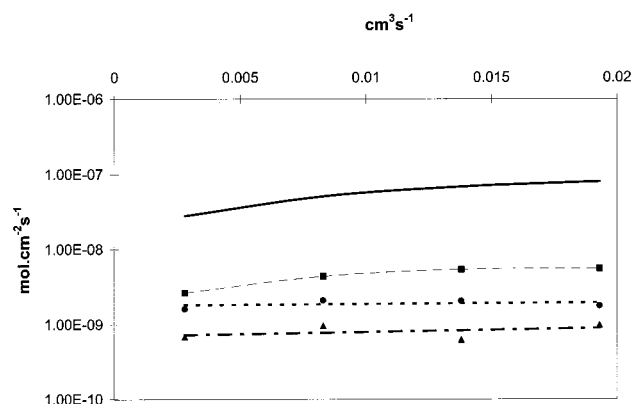


Figure 9. Change of the dissolution rate with the solution flow rate of (100) (■), (110) (●), and (111) (▲) MgO surfaces in 0.01 M HCl. The simulated dissolution rate (—) calculated assuming a proton diffusion-controlled reaction is shown.

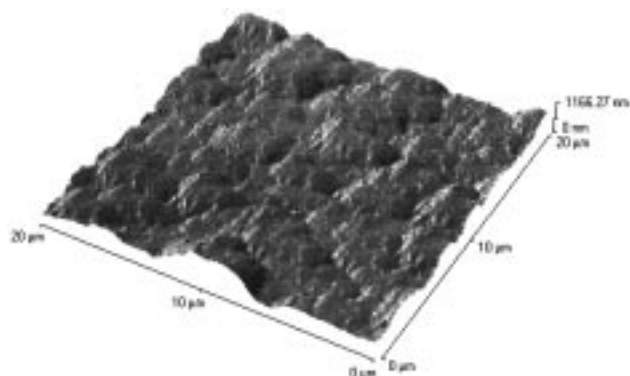


Figure 10. In-situ AFM image of the (110) MgO surface during dissolution in 0.01 M HCl and 0.01 M Mg(NO₃)₂.

rate of dissolution as measured from the average surface height does not change significantly. However, if we consider the perimeter of the pits, given by $4l$ for a square of side length l

TABLE 2: Rate of Pit Growth on the Surface (100) of MgO in 0.01 M Hydrochloric Acid

	velocity of pit growth
acid only	$1.7 \pm 0.1 \text{ nm s}^{-1}$
+0.1 M NaCl	$0.9 \pm 0.1 \text{ nm s}^{-1}$
+0.01 M Mg(NO ₃) ₂	$0.9 \pm 0.1 \text{ nm s}^{-1}$

and πd for a circle of diameter d , then we see that the perimeter growth rate for square $\langle 110 \rangle$ pits is 6.8 nm s^{-1} while for the circular pits it is 6.9 nm s^{-1} , so that the sets of data given in Tables 1 and 2 are seen to be mutually consistent. The formation of square $\langle 110 \rangle$ pits in preference to $\langle 100 \rangle$ pits can be understood on the basis of Figure 11a, which shows the crystalline structure of the (100) plane and the step and kink structure in the $\langle 100 \rangle$ and $\langle 110 \rangle$ direction. It can be seen that the removal of ions from the steps on the $\langle 100 \rangle$ direction requires the breaking of more ionic bonds than in the $\langle 110 \rangle$ direction, reflecting the different coordination in the plane of the ions to the surface (two against three).

We next address the apparent paradox that the change from square to circular pits on altering the solution pH is not accompanied by any change in the rate of the dissolution reaction. Consideration of Figures 11a and b show that this transition can be induced by the inhibition of the velocity of kink movement (V_k) and/or enhancement of the step movement (V_s). Since there is no overall change in the total dissolution rates, we must assume that the latter (V_s) is rate determining in both cases but the morphological transition is induced by retardation of V_k . Examination of Table 2 shows that both 0.1 M NaCl and 0.01 M Mg(NO₃)₂ can cause retardation of V_s , with the latter being especially potent, but since square pits are observed, the retardation must be insufficiently large relative to V_k so as to induce morphological change. Accordingly, the circular pits formed in 0.1 M HCl, in contrast to the square pits seen in 0.01 M HCl, must arise from the retardation of V_k due to proton adsorption. We can conclude, therefore, that H^+ is especially potent, as compared to the surface-active ions in Mg(NO₃)₂ or NaCl, in inhibiting the kink motion. At present,

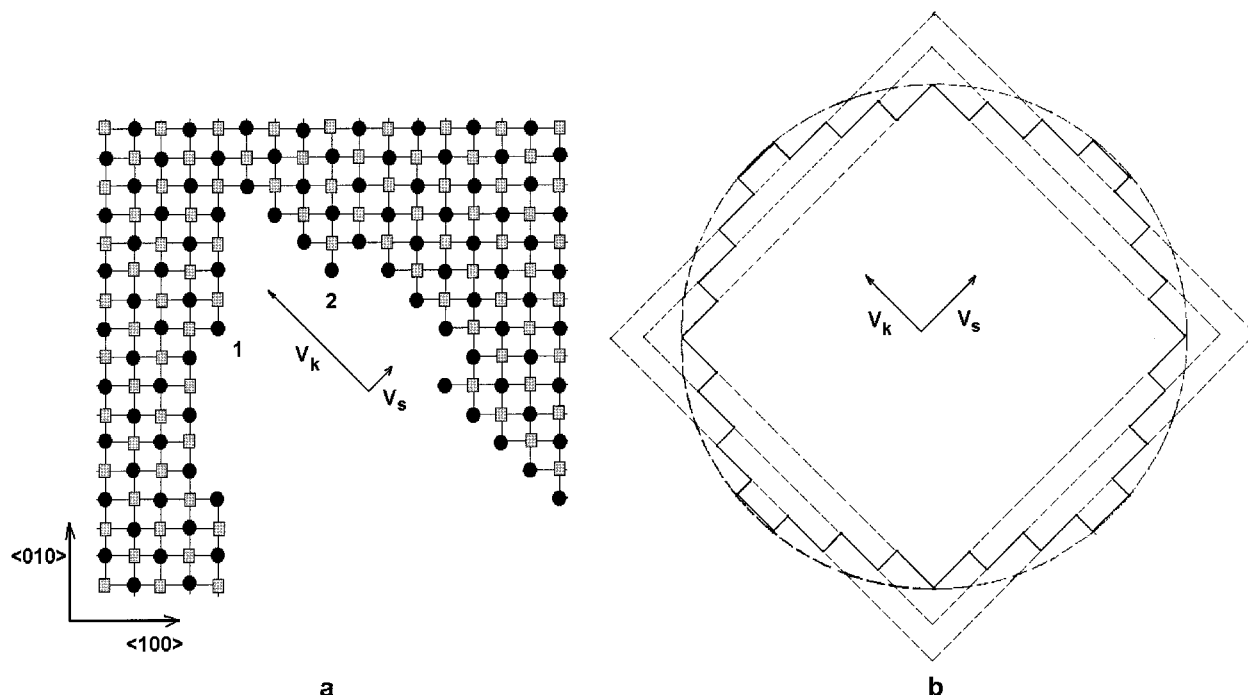


Figure 11. (a) Crystalline structure of the (100) plane of MgO, and the step and kink structure in the directions $\langle 100 \rangle$ (1) and $\langle 110 \rangle$ (2). The oxygen atoms are represented by the symbol ● and magnesium atoms by the symbol ■. (b) Model of the evolution of circular pits from square pits in the direction $\langle 110 \rangle$ by the inhibition of the velocity of kink movement (V_k) and/or enhancement of the velocity of step movement (V_s).

further speculation as to the precise structural interactions of these surface-active species is probably unwarranted but the area would benefit soon from further theoretical simulation studies.^{21,28–32}

Finally, we note that there is ample literature evidence^{11,21} for the stability of the (100) plane of MgO. This is further evidenced by our observations, thought to be original, of the formation of ridges on the (110) surface and triangular etch pits on the (111) surface formed by (100) planes during acid dissolution.

Acknowledgment. We thank COLCIENCIAS for a scholarship for M.F.S.

References and Notes

- (1) Macpherson, J. V.; Unwin, P. R. *Prog. React. Kinet.* **1995**, *20*, 186.
- (2) Unwin, P. R.; Macpherson, J. V. *Chem. Soc. Rev.* **1995**, 109.
- (3) Burton, W. K.; Cabrera, N.; Frank, F. C. *Philos. Trans. R. Soc. London, Ser. A* **1951**, *243*, 299.
- (4) Gratz, A. J.; Manne, S.; Hansma, P. K. *Science* **1991**, *251*, 1343.
- (5) Gratz, A. J.; Hiller, P. E.; Manne, S.; Hansma, P. K. *Geology*, **1992**, *20*, 359.
- (6) Hiller, P. E.; Manne, S.; Gratz, A. J.; Hansma, P. K. *Ultramicroscopy* **1992**, *42–44*, 1387.
- (7) Coles, B. A.; Compton, R. G.; Booth, J.; Hong, Q.; Sanders, G. H. *W. J. Chem. Soc., Chem. Commun.* **1997**, 619.
- (8) Coles, B. A.; Compton, R. G.; Suárez, M. F.; Booth, J.; Hong, Q.; Sanders, G. *Langmuir* **1998**, *14*, 218.
- (9) Hong, Q.; Suárez, M. F.; Coles, B. A.; Compton, R. G. *J. Phys. Chem. B* **1997**, *101*, 5557.
- (10) Vermilyea, D. A. *J. Electrochem. Soc.* **1969**, *116* (9), 1179.
- (11) Onishi, H.; Chikashi, C.; Aruga, T.; Iwasawa, Y. *Surf. Sci.* **1987**, *191*, 479.
- (12) Rácz, I.; Zelkó, R.; Bihari, E. *Drug Dev. Ind. Pharm.* **1996**, *22* (3), 225.
- (13) King, S. L.; Wilby, M. R.; Boyd, I. W. *Mater. Sci. Eng.* **1996**, *B37*, 162.
- (14) Jones, C. F.; Segall, R. L.; Smart, R. S. C.; Turner, P. S. *Rad. Eff.* **1982**, *60*, 167.
- (15) Topometrix Corp., Santa Clara, CA.
- (16) CRC, Handbook of Chemistry and Physics, 74th ed.; CRC Press: Boca Raton, FL, 1994.
- (17) Compton, R. G.; Pilkington, M. B. G.; Stearn, G. M. *J. Chem. Soc., Faraday Trans.* **1988**, *84* (6), 2155.
- (18) Sangwal, K.; Sutaria, J. N. *J. Mater. Sci.* **1976**, *11*, 2271.
- (19) Ghosh, T. K.; Clarke, F. J. P. *Brit. J. Appl. Phys.* **1961**, *12*, 44.
- (20) Sangwal, K.; Arora, S. K. *J. Mater. Sci.* **1978**, *13*, 1977.
- (21) Leeuw, N. H.; Watson, G. W.; Parker, S. C. *J. Phys. Chem.* **1995**, *99*, 17219.
- (22) Guspiel, J.; Riesenkauf, W. *Hydrometallurgy* **1993**, *34*, 202.
- (23) Jones, C. F.; Segall, R. L.; Smart, R. S. C.; Turner, P. S. *Proc. R. Soc. London* **1981**, *A374*, 141.
- (24) Kato, Y.; Tamashita, N.; Kobayashi, K.; Yoshizawa, Y. *Appl. Therm. Eng.* **1996**, *16* (11), 853.
- (25) Yuktaka, K.; Yamashita, N.; Kobayashi, K.; Yoshizawa, Y. *Appl. Therm. Eng.* **1996**, *16* (11), 853.
- (26) Furrer, G.; Stumm, W. 1986. *Geochim. Cosmochim. Acta* **1986**, *50*, 1847.
- (27) Ludwig, C.; Casey, W. H.; Rock, P. A. *Nature* **1995**, *375* (4), 44.
- (28) Refsori, K.; Wogelius, R. A.; Fraser, D. G.; Payne, M. C.; Lee, M. H.; Milman, V. *Phys. Rev.* **1995**, *B52* (15), 10823.
- (29) Langel, W.; Parrinello, M. *J. Phys. Chem.* **1995**, *103* (8), 3240.
- (30) Scamehorn, C. A.; Harrison, N. M.; McCarthy, M. I. *J. Phys. Chem.* **1994**, *101* (2), 1547.
- (31) Gibson, A.; Haydock, R.; LaFemina, J. P. *Phys. Rev. B* **1994**, *50* (4), 2582.
- (32) Gibson, A.; Haydock, R.; LaFemina, J. P. *J. Vac. Sci. Technol.* **1992**, *A10* (4), 2361.